Compound Droplet Modeling for Circulating Tumor Cell Microfiltration With Adaptive Meshing Refinement

Mohammad Abul Hashem
School of Engineering and Computer Science,
Washington State University,
Vancouver, WA 98686
e-mail: chenx@wsu.edu

Arian Aghilinejad
Department of Aerospace and
Mechanical Engineering,
University of Southern California,
Los Angeles, CA 90089

Xiaolin Chen
School of Engineering and Computer Science,
Washington State University,
Vancouver, WA 98686

Hua Tan
School of Engineering and Computer Science,
Washington State University,
Vancouver, WA 98686

Advances in microfluidics inaugurate a new possibility of designing diagnostic devices for early cancer detection. There is a growing interest in deformation-based microfiltration for capturing circulating tumor cells (CTCs) from peripheral blood due to its simplicity and low cost. Fundamental understanding of CTC passing through a microfilter is critical, as it helps optimize the design for achieving high isolation purity. Previous research has modeled CTC as a simple droplet for deformation-based CTC separation. Here, we use a compound droplet model to study the flow dynamics more realistically. An adaptive-mesh-refinement (AMR) method is used here, using the open-source code, GERRIS, after modification for droplet dynamics and contact angle model. The developed code is validated with results compared with ANSYS FLUENT and available theory. The effects of various parameters such as the nuclear-to-cytoplasmic (N/C) ratio, operating flow rate, and cell viscosity are investigated. It is found that the compound droplet behaves like a homogeneous droplet when the nucleus size is smaller than the filtering channel. However, the pressure profile is greatly influenced by the nucleus when it is larger than the channel size. In addition, there is a linear correlation between the pressure drop in the channel and the operating flow rate. Similarly, critical passing pressure increases linearly with the increase of the cell viscosity. Our study suggests that for having an accurate prediction of cell transport behavior inside the microchannel, it is of great importance to consider the effects of the nucleus and its possible deformation.
[DOI: 10.1115/1.4048134]

Keywords: circulating tumor cell, compound droplet model, adaptive-mesh-refinement (AMR), pressure profile, numerical simulation

1 Introduction

The lethality of cancer stems from metastasis, a term defined when malignant cells are released into the bloodstream and travel to distant organs to form secondary (distant) tumors [1]. These cancerous cells that exist in the circulatory system of patients are termed circulating tumor cells (CTCs). The importance of CTCs in cancer care and research is critical as their separation from patients' blood sample can be used for both cancer diagnosis and prognosis. Although CTCs are recognized as a potential biomarker for early cancer diagnostics, there is a major difficulty in separating them in the bloodstream due to the extreme rarity of these bioparticles. In recent years, microfluidic technologies are getting more and more popular to device CTC separation schemes. These devices take advantage of controlling mechanical, biological, and fluidic environment at the cellular scale [2,3]. Currently, many microfluidic separation schemes are focusing on label-free separation approaches, which utilizes the differences in intrinsic properties of CTCs rather than biological markers to separate these bioparticles. Common label-free separation approaches include deterministic lateral displacement [4], microfiltration [5,6], pinched flow fractionation [7], inertial separation [8], magnetophoresis [9], acoustophoresis [10], optical methods [11], dielectrophoresis [12,13], and combined techniques [14]. Among them, the deformation-based CTC separation method has shown promising capabilities regarding its simplicity, performance stability, and low cost [15]. In this method, CTCs are trapped by allowing more deformable blood cells to pass through a microfilter. The process of a cancer cell traveling through a microfilter is a complicated process, and there is extensive literature available on this topic. While some studies suggest that cancer cells may experience frequent and transitory nuclear envelope ruptures when they move through tight spaces over a timespan of hours or days [16]; here, we focus on cell passing event through microfilters in a timespan of few minutes which results in the adherence of the cancer cells only to the inner walls of bifurcation channel [17].

Along with the experimental studies, numerical simulation emerges as a powerful tool to predict the cell behavior inside a microfilter and to deliver important insights to optimize the processes. By examining the cell–channel interaction inside the microchip, numerical analysis methods can greatly contribute to the field by providing a fundamental understanding of CTC behavior inside the microfilter. One of the key challenges for numerical analysis of deformation-based microfiltration is the mechanical modeling of living cells. Generally, there are two main approaches in modeling the living cells: micro-/nanostructural approaches and continuum approaches. The micro-/nanostructural approaches consider subcellular interactions and are often expensive when used in the numerical simulation. Among different continuum models, the elastic shell model has shown promising results in providing responses to surface deformations, including shear, subcellular interactions, area dilation, and bending. However, the elastic model is generally inadequate for describing the mechanics of cells because the apparent elasticity of material will also depend on both the loading rate and loading history [18]. Different experiments have been conducted to analyze the blood cell aspiration through a micropipette. While the red blood cell response is dominated by the cell membrane, the white blood cell behaves like a highly viscous fluid drop, and

Contributed by the Fluids Engineering Division of ASME for publication in the JOURNAL OF FLUIDS ENGINEERING. Manuscript received February 12, 2020; final manuscript received July 23, 2020; published online September 4, 2020. Assoc. Editor: Yechun Wang.

the large viscosity of the cytoplasm dominates its response to external forces [19–21]. It was shown that when a constant suction pressure was applied, the cells flow continuously into a pipette with no apparent approach to a static limit. There is evidence that CTCs are more mechanically similar to white blood cells [22]. The cytoplasm of the CTC can be treated as a liquid, and its surface has a persistent cortical tension that causes the cell to assume a spherical shape.

Due to the efficiency in using liquid droplet model (as a continuum approach) for cell deformation problems in microfiltration devices [23], most of the previous studies used this model to investigate the behavior of the living cell in microfiltration channel [24,25]. Although it provides less insight at the subcellular level, the model is more straightforward when modeling the complex interactions between the cell, channel, and blood plasma during the microfiltration process. This model assumes that the cell consists of a homogeneous liquid encapsulated by a cortical membrane, where the cortical membrane is treated as a viscous fluid layer with constant surface tension. Several studies have been done by modeling the cell as Newtonian [26,27] and non-Newtonian [28,29] liquid droplet models, which provide valuable information regarding the cell behavior in microfilters. However, the morphometric measurement of Schmid-Schonbein et al. revealed that the nucleus is irregularly segmented and fills approximately 21% of the human cell volume [30]. Furthermore, the nucleus may occupy up to 75% of the cell volume for cancer cells [18]. The nuclear membrane is 3–4 times stiffer than the cortical membrane, and the nucleus is several times as viscous as the cytoplasm [31]. Thus, the interior of the cell is far from the homogenous nature in reality. Therefore, a more complex model is required to reflect the physical properties of the cell accurately.

Although the conventional modeling of the CTC as a simple liquid droplet provides useful information regarding the pressure profile, there is no comprehensive study to investigate the effect of the nucleus in compound structure of the CTC passing process inside the microfilter. Simulation of the flow physics of a compound droplet is challenging due to the two moving and deforming interfaces. There are valuable studies in the literature which used different methods such as the boundary element or diffuse interface methods to conduct compound droplet modeling. Luo et al. studied the deformation behavior of an elastic capsule in shear flow using the front-tracking method [32]. Smith et al. used a level-set method to investigate the behavior of a viscous compound droplet in shear flow, focusing on the influence of the relative magnitude of the surface tensions of the two interfaces [33]. Using a three-dimensional (3D) spectral boundary element method, Qu and Wang investigated the motion, deformation, and stability of a viscous compound droplet in a planar extensional flow [34]. They observed that given the same mechanical properties, both the inner and out droplets undergo significant deformation if the inner droplet is larger. Wang et al. investigated the rheological behaviors of an eccentric compound droplet in a modest extensional flow using spectral boundary element methods [35]. They observed that the shift of a compound droplet is driven by the asymmetric interfacial curvature instead of just by the asymmetric outer drag. Zhou et al. developed a diffuse-interface method and investigated the morphological evolution of a compound droplet as it moves through a contraction tube under a fixed pressure difference [36]. They observed that the nucleus hinders the deformation of the compound droplet and increase the transit time. While these studies are providing insight in cell behavior, literature still lacks a systematic study to investigate the role of nucleus size and properties in cell entry behavior inside the microfilters.

In this study, the CTC is modeled as a compound droplet to consider the effects of nucleus size during cell aspiration. This is a shift from previous CTC modeling studies existing in the literature treating the CTC as a single-phase droplet (simple droplet) [25,29]. In the compound droplet model, we are dealing with a multiphase flow problem involving three immiscible liquid phases separated by two interfaces. Hence, the passing event of a CTC through the microfilter consists of complex hydrodynamics of the two moving and deforming interfaces and the microfiltration wall. The fluid domain of interest here contains three phases: the nucleus, cytoplasm, and the blood as the carrier fluid. To study the pressure signature in the microfiltration, we use the volume of fluid (VoF) method to track the blood–cytoplasm and cytoplasm–nucleus interfaces. Compared to other methods, the VoF method does not require semianalytically solving integral equations involving kernel functions as in the boundary element approach. It does not allow an interface between the phases to have a nonzero thickness either, i.e., a diffuse-interface. Further, it uses volumetric data to store interface location, and the conservation of volume is guaranteed.

Studying this complex multiphase interaction with VoF requires an essential need for high grid resolution at the cell-wall interface. So far, most of the previous studies on the passing event of the cell inside the microfiltration channel are based on the static computational grid that is defined at the beginning and cannot be modified throughout the computation [25,29,37]. Using a static grid requires an increase in global mesh density, which leads to extensively high computational costs, especially when dealing with the compound droplet model with three immiscible phases involved. In this study, to address this challenging issue, an open-source code Gerris [38] has been modified for the droplet dynamics during cell squeezing. The developed code enables us to concentrate the computational effort on regions where more accuracy is needed through the AMR strategy. The effects of different parameters are investigated such as nuclear to cytoplasmic (N/C) ratio, flow rate, and viscosities of the cytoplasm and nucleus in the cell entry event. The cell evolution and pressure profiles during passing through the microchannel are studied and discussed in detail. Our article is organized as follows. In Sec. 2, we present the operation principle of the deformation-based CTC filtering device, numerical method, and model settings. Numerical method validation is presented in Sec. 3 with the theoretical background. Section 4 covers a detailed discussion of our findings. In Sec. 5, we discuss the model limitations and future work. Section 6 is the conclusion.

2 Methodology

2.1 Operation Principle. The device filtering process is based on the flow of sample blood cells through a filtering channel where they can be separated due to their different deformations. There is a critical pressure defined as a pressure needed for each cell to squeeze through the microfilter, which highly depends on the cell deformability and diameter. The more deformable and smaller cells (normal blood cells) can simply pass the channel, whereas the stiffer and larger ones (CTCs) are required to overcome the critical pressure and can be blocked due to the lack of sufficient external pressure. In this research, the cell is described as a cortical shell-liquid drop where its ability to resist deformation is due to the surface energy (interfacial tension) of the droplet [18]. CTCs, like other eukaryotic cells, are composed of the cortical membrane, cytoplasm, and a nucleus. It has been shown that the nucleus is many times stiffer and more viscous than the surrounding cytoplasm [26,31]. Hence, it is important to include these mechanical properties in the analysis for achieving a fundamental understanding of cell behavior inside the microchannel.

In this study, the CTC is modeled as a compound two-phase (nucleus and cytoplasm) viscous liquid droplet with a perfect spherical shape before squeezing process. The cell is encapsulated by an infinitely thin cortical membrane with constant surface-tension, as illustrated in Fig. 1. It is composed of the cytoplasm and the nucleus, which are both considered as Newtonian fluids. The basic design geometry of the proposed microfilter is also shown in Fig. 1. The device is mainly composed of three sections: entrance chamber, filtration channel, and exit chamber. The entrance and exit chamber have an identical configuration with a

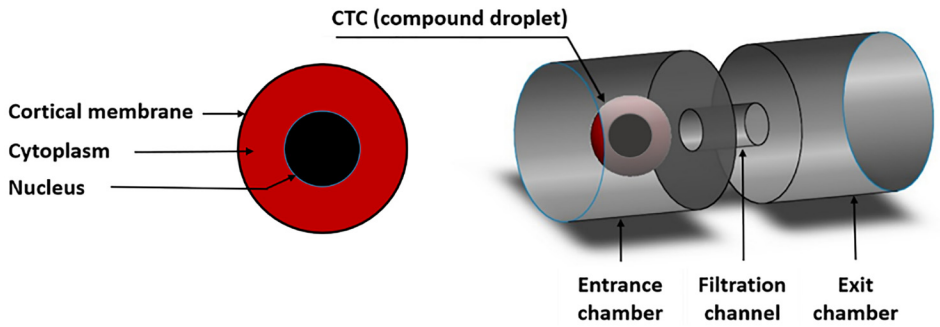

Fig. 1 CTC compound droplet model and microfilter configuration

radius of 15 μm while the radius of the filtration channel is 4 μm. The length of the entrance and exit chambers are identical and set to be 30 μm. The length of the filtration channel is 15 μm.

2.2 Numerical Method. The multiphase flow in the microfilter is governed by the continuity and Navier–Stokes (NS) equation and the VOF method for the phase transport equation as follows:

$$\nabla \cdot \boldsymbol{u} = 0 \tag{1}$$

$$\rho\frac{\partial \boldsymbol{u}}{\partial t} + \rho(\boldsymbol{u}\cdot\nabla)\boldsymbol{u} = \nabla\cdot\left[-p + \mu\left(\nabla\boldsymbol{u} + (\nabla\boldsymbol{u})^T\right)\right] + \sigma\kappa\delta_s\boldsymbol{n} \tag{2}$$

$$\frac{\partial(C)}{\partial t} + \nabla\cdot(\boldsymbol{u}C) = 0 \tag{3}$$

where **u** is velocity vector, p is pressure, σ is surface tension coefficient, κ and n are the curvatures and the unit normal vector of the interface, respectively, and δ_s is Dirac distribution function. The surface tension force, $\sigma\kappa\delta_s\boldsymbol{n}$ is included as a body force term in momentum equations [39]. The VOF method is adopted to track the sharp interface between different phases with a volume fraction variable $c(x,t)$ varying from 0 to 1. For the computational location inside the interface $c = 1$, and for the location outside of the interface $c = 0$. When a grid cell contains both phases, i.e., there is an interface between two phases, then $0 < c < 1$. Since the VOF method does not track the exact location of the surface in the Lagrangian sense, the interface is reconstructed implicitly from the volume fraction piecewise-linear interface calculation (PLIC) method. In this method, the linear function $\boldsymbol{n}\cdot\boldsymbol{x} = \alpha$ is used to represent each interface segment, where $\boldsymbol{n}$ is the normal vector of the interface calculated by the height-function method [40] or $\nabla c/|\nabla c|$ using the mixed Youngs-centered method [41], and α is calculated using the normal vector and volume fraction [42].

As mentioned in Sec. 2.1, the cell is modeled as a compound droplet of three phases defined as φ_b, φ_c, and φ_n for blood, cytoplasm, and nucleus (nucleoplasm), respectively. Therefore, this study deals with two different interfaces, one between blood and cytoplasm (Ψ_{bc}) and the other one between cytoplasm and nucleoplasm (Ψ_{cn}), as shown in Fig. 2. To track the interfaces, we use two VOF variables: c_1 for tracking Ψ_{bc} and c_2 for tracking Ψ_{cn}. Density ρ and viscosity μ of the fluid are dependent on volume fraction field as follows:

$$\rho = \begin{cases} c_1\rho_b + (1-c_1)\rho_c, & \text{for } \varphi_b \text{ and } \varphi_c \\ c_2\rho_c + (1-c_2)\rho_n, & \text{for } \varphi_c \text{ and } \varphi_n \end{cases} \tag{4}$$

$$\mu = \begin{cases} c_1\mu_b + (1-c_1)\mu_c, & \text{for } \varphi_b \text{ and } \varphi_c \\ c_2\mu_c + (1-c_2)\mu_n, & \text{for } \varphi_c \text{ and } \varphi_n \end{cases} \tag{5}$$

where ρ_b, ρ_c, ρ_n and μ_b, μ_c, μ_n are the densities and viscosities of the blood, cytoplasm, and nucleus, respectively. Note that $c_1 = 1$ represents the cytoplasm domain (φ_c), $c_1 = 0$ represents the blood domain (φ_b) and $0 < c_1 < 1$ represents the interface of the cytoplasm and blood (Ψ_{bc}). Similarly, $c_2 = 1$ demonstrates the nucleus domain (φ_n), $c_2 = 0$ represents the cytoplasm domain (φ_c) and $0 < c_2 < 1$ represents the interface of the cytoplasm and nucleus (Ψ_{cn}). The open-source AMR code GERRIS [38,43] is used for solving multiphase flows with surface-tension effect. The octree-based (quadtree in two-dimensional (2D)) AMR [44] in GERRIS makes the computational grid adaptive to either or the combination of the curvature, critical locations, variables and their gradients, or user-defined functions. The AMR allows the concentration of the computational effort in the regions where it is needed most and hence leads to accurate solutions at a much less computational cost [38,43].

The surface tension of the cortical and nuclear membrane is modeled by the continuum surface force (CSF) method [39]. GERRIS solves the Navier–Stokes (NS) equations using a finite volume-based time-splitting projection method on the Cartesian grid. As the numerical methods in GERRIS are well reported in Refs. [38,43], here we only give a brief overview. The NS equations are discretized as

$$\rho^{n+1/2}\left[\frac{u^{n+1}-u^n}{\Delta t} + (u^{n+1/2}\cdot\nabla)u^{n+1/2}\right] = -\nabla p^{n+1/2} + \nabla\cdot\left[\mu^{n+1/2}(D^n + D^{n+1})\right] + (\sigma\kappa\delta_s n)^{n+1/2} \tag{6}$$

where $D = (\nabla u + \nabla u^T)/2$ is the deformation tensor, Δt is the increment of time-step, and the superscript denotes the time-step number. Equation (6) is solved using a fractional-step projection method. First, a provisional velocity u^* is given by

$$\rho^{n+1/2}\left[\frac{u^* - u^n}{\Delta t} + (u^{n+1/2}\cdot\nabla)u^{n+1/2}\right] = -\nabla p^{n+1/2} + \nabla\cdot\left[\mu^{n+1/2}((2-\beta)D^n + \beta D^*)\right] + (\sigma\kappa\delta_s n)^{n+1/2} \tag{7a}$$

In the next step, the u^{n+1} can be obtained by correcting the provisional velocity u^* as

$$u^{n+1/2} = u^* - \frac{\Delta t}{\rho^{n+\frac{1}{2}}}p^{n+1/2} \tag{7b}$$

The parameter β determines the numerical scheme for the viscous term in NS equations, i.e., $\beta = 0$ yields an Euler-forward explicit scheme, $\beta = \frac{1}{2}$ yields a second-order, Crank–Nicholson implicit scheme, $\beta = 1$ yields a first-order, Euler-backward implicit scheme. Note that in our numerical method, the advection term is calculated using second-order conservative Gudonov method. Finally, the pressure $p^{n+1/2}$ is obtained by taking the divergence of Eq. (7*b*) and using the incompressibility constraint [45]. The surface tension force $(\sigma\kappa\delta_s n)^{n+1/2}$, can be written in form of gradient of volume fraction $c(\boldsymbol{x},t)$ as

$$(\sigma\kappa\delta_s n)^{n+1/2} = \sigma\kappa^{n+1/2}\nabla c^{n+1/2} \tag{7c}$$

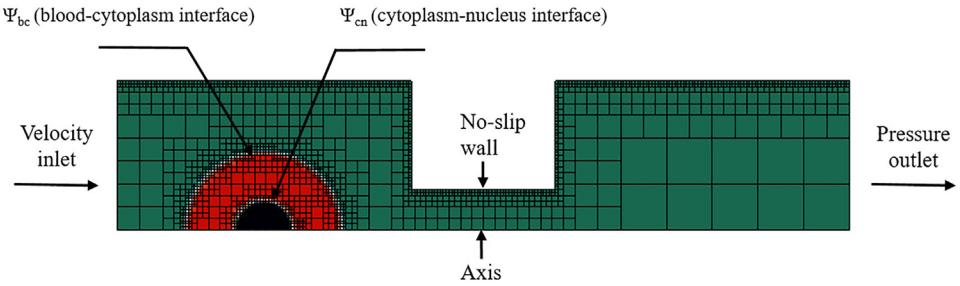

Fig. 2 Two-dimensional axisymmetric mesh structure of the computational domain. AMR is employed in the critical regions, say, two moving interfaces and the solid boundary.

Table 1 Parameters for compound CTC modeling

Parameter	Dimensions	References
CTC radius	8 μm	[25]
Nucleus radius	2–6 μm	[23,30]
Surface tension coefficient of cortical membrane, σ_c	50 mN/m	[47]
Surface tension coefficient of nuclear membrane, σ_n	200 mN/m	[48]
Blood viscosity, μ_b	0.001 Pa·s	[49]

Table 2 Parameter settings for different case study

Section	Cytoplasm viscosity, μ_c (Pa·s)	Nucleus viscosity, μ_n (Pa·s)	*N*/*C* ratio	Inlet velocity, *U* (m/s)	Flow rate, *Q* (nL/s)
4.1 Effects of *N*/*C* ratio	0.001	0.01	0.25, 0.38, 0.55,0.75	0.02 [37]	14
4.2 Effects of flow rate	0.001	0.01	0.25, 0.38, 0.55, 0.75	0.01–0.2	7–141
4.3 Effects of viscosity	0.001-0.01	10 μ_c	0.25, 0.55, 0.75	0.02	14

where the curvature κ is estimated using a height-function-based hierarchical method [38]. The numerical stability is ensured by controlling time-step size (Δt) using the Courant–Friedrichs–Lewy (CFL) condition and the shortest capillary wave due to explicit treatment of surface tension force as following [38]:

$$\Delta t = f_{CFL} \min\left(\frac{\Delta}{|u_i|}, \frac{\rho\Delta^2}{\mu}, \sqrt{\frac{\rho\Delta^3}{\sigma}}\right) \tag{8}$$

where Δ is the minimum cell size, u_i is the cell- or face-centered velocity in i-direction, f_{CFL} is CFL number, and set to 0.5 in this study. The wetting or wall-adhesion effect, i.e., the interaction between the liquid and solid surface, plays an important role in the cell-squeezing process. In this study, we assume the contact angle to be a constant regardless of the movement of the contact line. We proposed a height-function-based contact angle model and implemented it in GERRIS for treating moving contact lines at the liquid–solid interface. The details of our model can be found in Refs. [45,46].

2.3 Model Description. The three-phase flow problem of concern in this study involes an axisymmetric geometry with a spherical cell centered along the centerline of a cylindrical-shaped microfilter. Figure 2 represents the mesh structure of the computational domain with the applied boundary conditions. For the incompressible three-phase flow, a constant velocity inlet boundary condition is set at the entrance of the microfilter, and the pressure outlet boundary condition is applied at the exit. The ambient reference pressure at the outlet is set as zero. No-slip, nonwetting boundary conditions are prescribed on the channel walls. The mesh of the computation domain in FLUENT simulation consists of about 33,500 quadratic elements, with the minimum element size 0.09 μm. The grid convergence study has been carried out to show that the grid size is small enough to generate grid-independent results. Parameter settings for the baseline design study of the compound CTC model are listed in Table 1.

Living cells are mainly consisting of the cell membrane, cytoplasm, and the nucleus. The cytoplasm contains a large percentage of water with granules, proteins, filamentous components, mitochondria, etc., where the presence of these elements greatly influences the biophysical behavior of the cell. In malignant tumor cells, the biophysical properties exhibit a wide range of variations depending on the cancer type, stage of cancer, and even from patient to patient. The volumetric ratio of the nucleus to the cytoplasm, often referred to as *N*/*C* ratio, also varies in different types of cancer cells. *N*/*C* ratio is considered as an important risk factor for some kinds of cancer. Hence, to achieve a realistic prediction about the cell's transport behavior in microfiltration channels, it is important to consider the effects of different biophysical properties of CTCs. In this work, we first studied the effects of nucleus size in the microfiltration channel by considering different *N*/*C* ratios. Then, the effects of flow rates on CTCs' motion behavior are studied. As the cell cytoplasm contains mainly water, we set the viscosity of the cytoplasm similar to the viscosity of water (0.001 Pa·s) as a baseline case. Finally, the effect of cytoplasm viscosity ranging from 0.001 to 0.01 Pa·s is investigated while the nucleus viscosity is considered to be ten times [49] higher than the cytoplasm viscosity. Parameters used in different sections of this study are listed in Table 2.

3 Numerical Method Validation

3.1 Theory Background. In the deformation-based microfilter, the CTC is pushed through the filtration channel by the operating pressure imposed at the inlet of the microfilter. The variation

of the operating pressure with respect to time is termed as the pressure profile, which conveys important signatures of the CTC passing process. The pressure is used to overcome the resistance caused by the surface tension of the cell and viscous resistance in the microfilter. Thus, the total pressure can be expressed as

$$P_t = P_{sur} + P_{vis} \tag{9}$$

where P_{sur} and P_{vis} represent the pressure to overcome the surface tension and the viscous resistance in the microfilter, respectively. For lower flow rates, the initial stage of the cell squeezing into the filtration channel can be approximated by a quasi-static aspiration process. In this case, we can assume that the aspirated part and nonaspirated part of the cell is spherical during squeezing through the microfilter.

The surface-tension-induced pressure P_{sur} can be estimated by the Young–Laplace equation as follows:

$$P_{sur} = 2\sigma\left(\frac{1}{r_{ch}} - \frac{1}{r_{cell}}\right) \tag{10}$$

where σ is the surface tension coefficient, r_{ch} and r_{cell} are curvature radii of aspirated and nonaspirated part of the interface during the squeezing process, respectively (as shown in Fig. 3). For pressure-driven flow in the microchannel, the major viscous pressure drop is due to the viscous resistance caused by fluid viscosity. During the cell constriction at the inlet and the expansion at the exit of the filtration channel, there are some minor pressure drops [50]. Total viscous pressure drop P_{vis} can be calculated using the following equation:

$$P_{vis} = \frac{8\mu LV}{r_{ch}^2} + K_c\frac{\rho V^2}{2} + K_e\frac{\rho V^2}{2} \tag{11}$$

where ρ and μ are the density and viscosity of blood plasma, respectively, L is the length of the filtration channel, V is the local flow velocity, K_c is the constriction coefficient, and K_e is the expansion coefficient. K_c and K_e are set as 0.5 and 1, respectively, assuming the filtering channel is much smaller than the filtering chambers. In this study, we will compare our numerical results with the theory described previously.

3.2 Validation. The original code GERRIS has been widely used in modeling of microscopic multiphase flows and has been validated with theory and experimental data for surface-tension-dominated flows in a variety of applications [45]. Here, we focus on validating our modified version of GERRIS for modeling a CTC-squeezing process through a microfilter. To the best of our knowledge, there is no existing theory to predict the pressure drop in the microfluidic channel for the compound droplet model. Hence, we modeled CTC as a simple droplet excluding the nucleus and compare results predicted from GERRIS against the results from the commercial CFD package ANSYS FLUENT. It should be noted that the adaptive mesh refinement setting could have been used in ANSYS FLUENT for a better comparison. However, since the goal of the comparison is to verify the modified GERRIS code's ability to produce accurate results, using the static mesh setting for ANSYS models would be adequate. In addition, we compared the numerical results from GERRIS with the theoretical prediction based on the simple droplet model. In this model, the effects of the nucleus are disregarded, and the properties inside the cell are chosen based on the cytoplasm. In terms of the flow equations, the general properties can be calculated using the volume fraction weighted average method. For instance, the density at an arbitrary node can be written as

$$\rho = \alpha_{cell}\rho_{cell} + (1 - \alpha_{cell})\rho_{medium} \tag{12}$$

where α_{cell} is the volume fraction of the cell ($\alpha_{cell} = 0$ in medium, $\alpha_{cell} = 1$ in the cell, and $0 < \alpha_{cell} < 1$ at the interface). All the simulations are 2D axisymmetric and run on an InfiniBand-connected HPC cluster (21 computing nodes, each node with 4 CPUs, 8 GB RAM, and 100 GB hard drive). As the simulation time depends on the flow rate specified at the inlet boundary of the microchannel, the computational time varies for cases with different flow rates. For the case of lower flow rates (e.g., 7 nL/s), it takes about 24 h for FLUENT to finish the simulation, whereas the calculation time decreases significantly to 40 min using GERRIS. For the case of higher flow rates (e.g., 141 nL/s), the simulation takes about an hour in ANSYS FLUENT while it takes only 10 min in GERRIS.

As the droplet passes the large portion of the computational domain during the squeezing process, the mesh is nearly uniform throughout the domain except for the boundaries (Fig. 4). The finer mesh is placed along the walls of the microfilter and symmetry axis to improve the accuracy of the simulation. The VoF method is adopted to track the cell interface, and surface tension is modeled by the CSF method.

Due to the adaptive meshing capability, GERRIS allows efficient mesh generation by concentrating meshes only in the critical regions according to flow features. We carried out grid independent study by setting the finest mesh levels at 6, 7, 8, and 9, which corresponds to the finest grid sizes of 1.17, 0.59, 0.29, and 0.15 μm, respectively. Simulation time taken for these refinement levels is 2, 5, 39, and 254 min, respectively. Typical simulation results (cell evolution) obtained from structured mesh settings (ANSYS FLUENT) and adaptive mesh settings (GERRIS) are presented in Fig. 5. The pressure/evolution results obtained from the simulation in GERRIS is shown in Fig. 6(*a*) and the percentage of difference of P_{sur} between numerical simulation and the theoretical value is shown in Fig. 6(*b*) for different mesh sizes.

As one can see, the surface-tension-induced pressure P_{sur} reaches the expected value with the increase of mesh size. However, the finest level is set to 8 in our study, which gives a good balance between accuracy and computational cost. To be mentioned that in the GERRIS code, the mesh is adaptive to the moving interfaces, velocity, and pressure gradient throughout the solution.

To validate the code, we simulated the squeezing process of the cell in different flow rates ranging from 7 to 35 nL/s. Figure 7 plots the inlet pressure history for flow rates $Q = 14$ and 21 nL/s obtained from GERRIS and ANSYS FLUENT, respectively. As we can see, the main features (e.g., peaks and valleys) of the pressure history predicted from the two codes are in very good agreement despite the minor difference in time progression. It is noticeable that such difference reduces with the increase in flow rate. A slight discrepancy is observed in the minimum pressure regions which occur during cell squeezed out of the filtration channel. The points g_1, f_1, and g_2, f_2 in the pressure profiles represent the critical

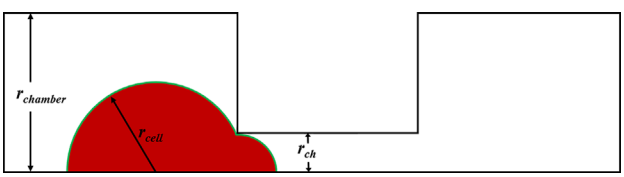

Fig. 3 CTC passing through the microfilter. For lower flow rates, leading and trailing edges of the cell remain spherical.

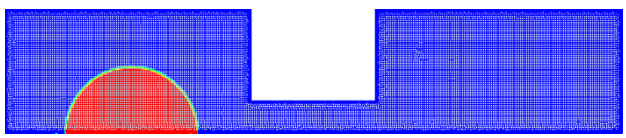

Fig. 4 2D axisymmetric mesh structure of the geometry in FLUENT

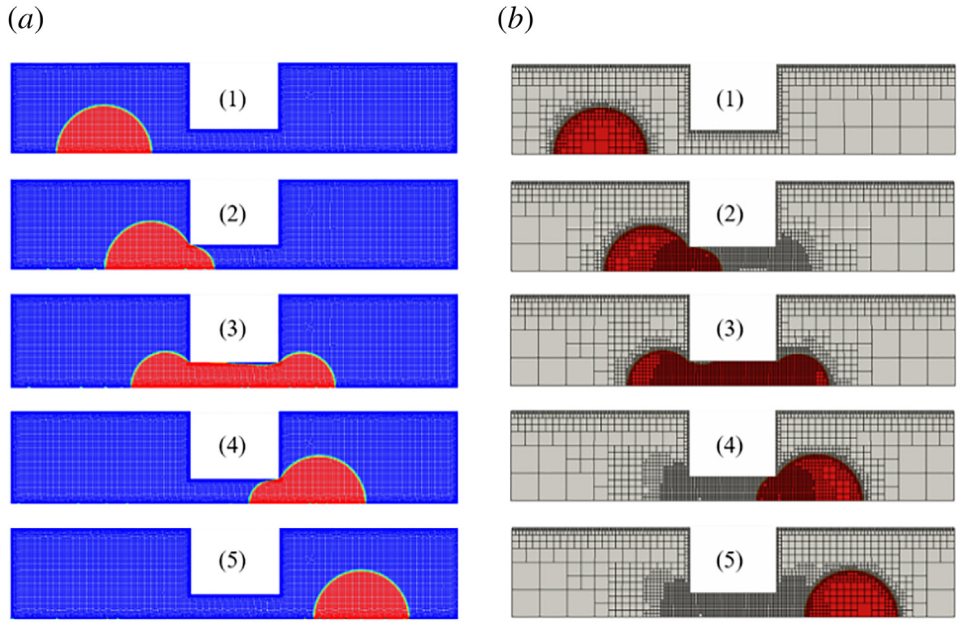

Fig. 5 Cell evolution in (*a*) structured mesh settings (ANSYS FLUENT) and (*b*) in adaptive mesh settings (GERRIS)

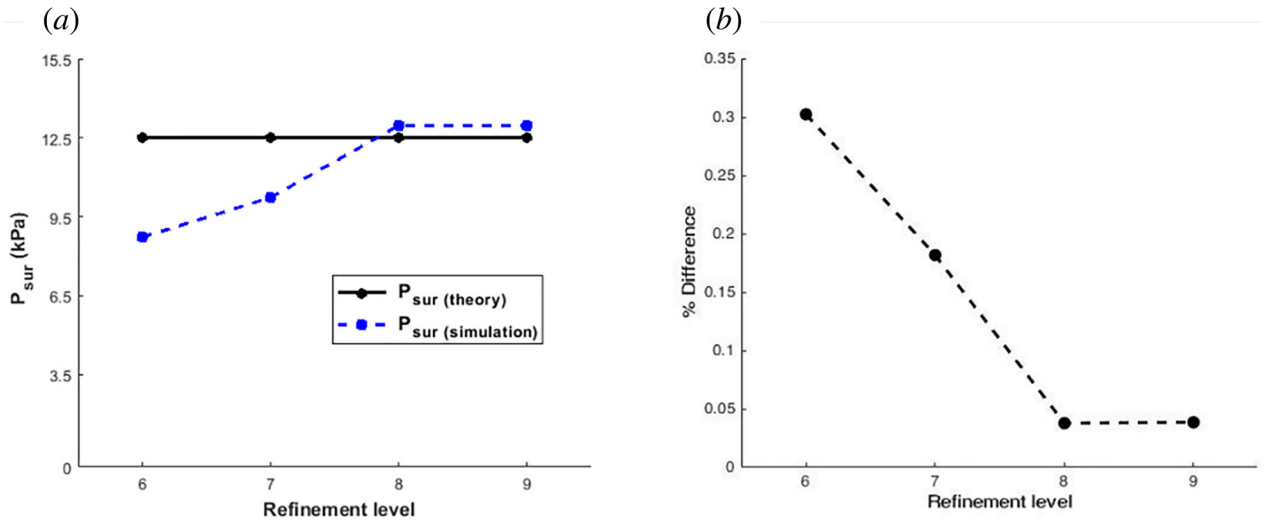

Fig. 6 (*a*) Evolution of surface-tension-induced pressure P_{sur} with the mesh size for $Q = 7$ nL/s, (*b*) Percent difference of P_{sur} between numerical simulation and the theoretical value corresponding to mesh refinement level

pressure, which is defined as the maximum pressure required for the cell to squeeze through the filtration channel.

For the case of low flow rates, the squeezing process can be considered as a quasi-static aspiration process, hence surface-tension-induced pressure P_{sur} follows the Young–Laplace equation (Eq. (10)). Viscous pressure P_{vis} is predicted by Eq. (11). The predicted P_{sur} from Eq. (10) is 12.5 kPa based on the initial droplet diameter and channel radius irrespective of the flow rates. Figure 8 depicts the comparison of P_{sur} and P_{vis} predicted from GERRIS, ANSYS FLUENT, and the theory (Eqs. (10) and (11)) for different flow rates. For flow rates $Q \leq 28$ nL/s, the surface-tension-induced pressure P_{sur}, has a good agreement with the theory, with an average relative error of 12% between GERRIS and theory, and 16% between FLUENT and theory, respectively. For $Q \geq 28$ nL/s, there is a deviation from the theoretical value. Both GERRIS and FLUENT predicted a surface-tension-induced pressure P_{sur} of 18.2 kPa at $Q = 35$ nL/s, which is deviating from the theoretical value of 12.2 kPa for about 50%. The large relative errors are as expected, especially at higher flow rates, as the initial aspiration deviates significantly from the hemispherical shape, which is an oversimplified assumption in theory. The deviation from the theoretical assumption becomes more substantial with increasing flow rates, and the theoretical equation for estimating the surface-tension-induced pressure can serve only as rough estimates or guidelines. P_{sur} obtained from the simulation results of GERRIS and ANSYS FLUENT agree well. P_{vis} predicted by the two codes also agrees well with the theory except for a small deviation. The deviation could be due to the cell deformation and interaction of carrier fluid with the cell, which has not been considered for the simplicity of the theory. To be mentioned that we have not observed any cell rupture under the prescribed flow conditions. Husson and coworkers [51] have characterized the mechanical criterion for the rupture of the cell membrane under compression via novel tilted microindentation technique. They have introduced a mechanical criterion for

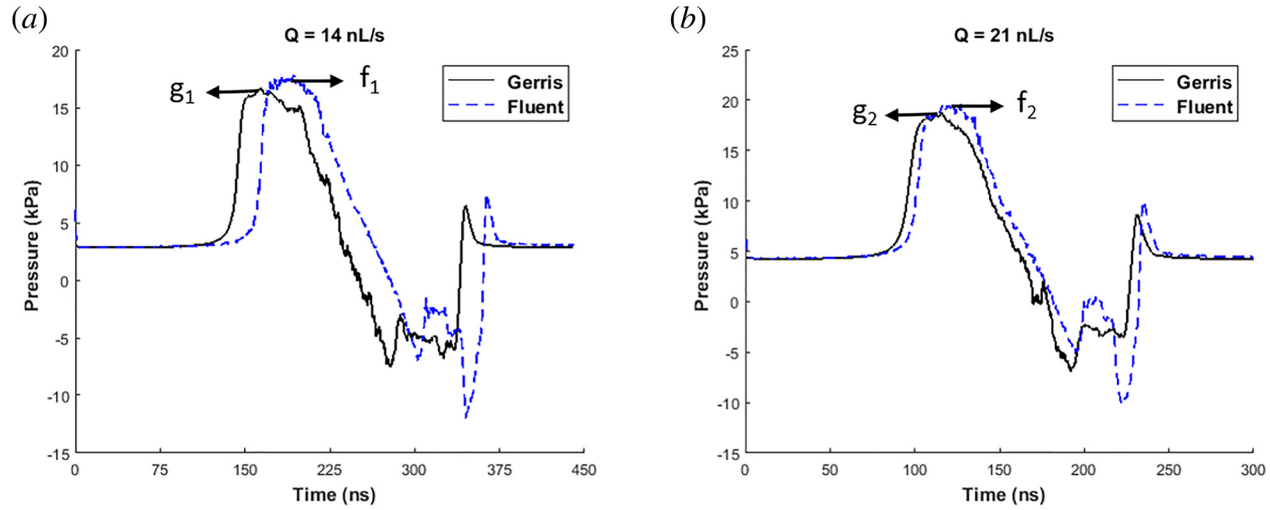

Fig. 7 Pressure profiles for cell-squeezing process simulated in our developed GERRIS code and commercial code ANSYS FLUENT: (*a*) $Q = 14$ nL/s and (*b*) $Q = 21$ nL/s. Pressure profiles show a good agreement between two codes with a relative error of 5% between the two predicted critical pressures at both $Q = 14$ nL/s and $Q = 21$ nL/s.

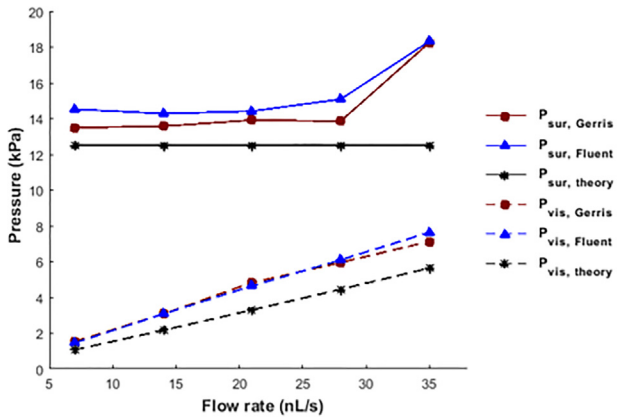

Fig. 8 Surface-tension-induced pressure, P_{sur}, and viscous pressure, P_{vis} for different flow rates. For flow rates $Q \leq 28$ nL/s, P_{sur} agrees well with Eq. (10), with the simulated values deviating from Eq. (10) for about 12% for GERRIS and 16% for FLUENT on average. For $Q = 35$ nL/s, due to the lack of spherical aspiration, simulated P_{sur} deviates about 50% from the theoretical P_{sur} value.

endothelial cell rupture, which is around constant normal stress of 12.4 kPa. Although in this study, we modeled a CTC with high surface tension, still the pressure peak as the CTC is experiencing in the microfiltration device is not significantly higher than the one that cell experiences under physiological condition.

The comparison of droplet shape evolutions predicted by GERRIS and ANSYS FLUENT is plotted in Fig. 9, which clearly shows a good match between the two results. A large relative error between GERRIS and FLUENT occurs when the cell is starting to block the channel. The large relative error of 23% at $t = 170$ μs for $Q = 14$ nL/s is mainly caused by the slight time shift in the predicted time history results between GERRIS and FLUENT simulations, as can be seen from the comparative pressure history profiles plotted in Fig. 7. Detailed discussions on the relation between the inlet pressure and droplet deformation profile will be presented in Sec. 4.

4 Results and Discussion

4.1 Effects of *N*/*C* Ratio. In this section, focusing on the relative size of the nucleus over the cytoplasm, the pressure profile and cell evolution are studied for different *N*/*C* values. Note that the pressure profile refers to the time history of total pressure at the inlet when a cell is squeezing through the microfilter. We modeled the CTC with nucleus size smaller (2 and 3 μm), comparable (4.4 μm), and larger (6 μm) than the filtration channel, resulting in *N*/*C* ratios of 0.25, 0.38, 0.55, and 0.75, respectively. Viscosity ratio is set as $\mu_b:\mu_c:\mu_n = 1:1:10$. The effects of the nucleus smaller and larger than the channel size are discussed separately in this section. In Figs. 10(*a*) and 10(*b*), the nucleus is smaller than the size of the filtration channel (*N*/*C* ratio 0.25 and 0.38, respectively), which results in a similar pressure profile with identical stages of the filtration process. Since the small nucleus does not deform during the squeezing process, it does not contribute to the pressure profile. Before entering into the filtration channel, the cell experiences viscous resistance, and the pressure remains constant at the entrance chamber (stages a1 and a2). As the cell starts squeezing through the filtration channel, there is a sudden rise in pressure due to the increase in surface-tension-induced pressure P_{sur} (stage b1). While the surface tension of the cell membrane keeps the shape of the cell, additional pressure is required to deform the cell for initial aspiration. The pressure reaches its maximum level during the initial aspiration or when the cell blocks the entrance of the filtration channel. The maximum pressure is termed as the critical pressure P_{cr} required for a CTC to squeeze through the filtration channel. After stage b1, the radius of the trailing edge of the cell starts decreasing, and the leading edge starts occupying the filtration channel. During the cell occupation stage (stages b1–b5), pressure gradually decreases following Eq. (10). At stage b2, surface-tension-induced pressure tends to zero since the radii of both edges are equal, and total pressure reaches to the level of viscous pressure. As the leading edge starts recovering the initial shape, P_{sur} changes direction, and the pressure gradually decreases until reaching a minimum value. Minimum pressure occurs when the trailing edge of the cell achieves a minimum radius of curvature before leaving the inlet chamber (stage b3). At the entrance of the filtration channel, the trailing edge has a larger radius of curvature and results in a local peak. Before the cell leaving the filtration channel, another local dip value is observed in the pressure profile at stage b5. At stage c1, when the cell completely leaves the filtration channel, there is a local peak that arises due to the bouncing of the trailing edge caused by inertia. In the exit chamber (stage c2), the pressure reaches the same level as that of the entrance chamber, and the CTC recovers its original spherical shape. Note that the nucleus smaller than the filtration channel size does not

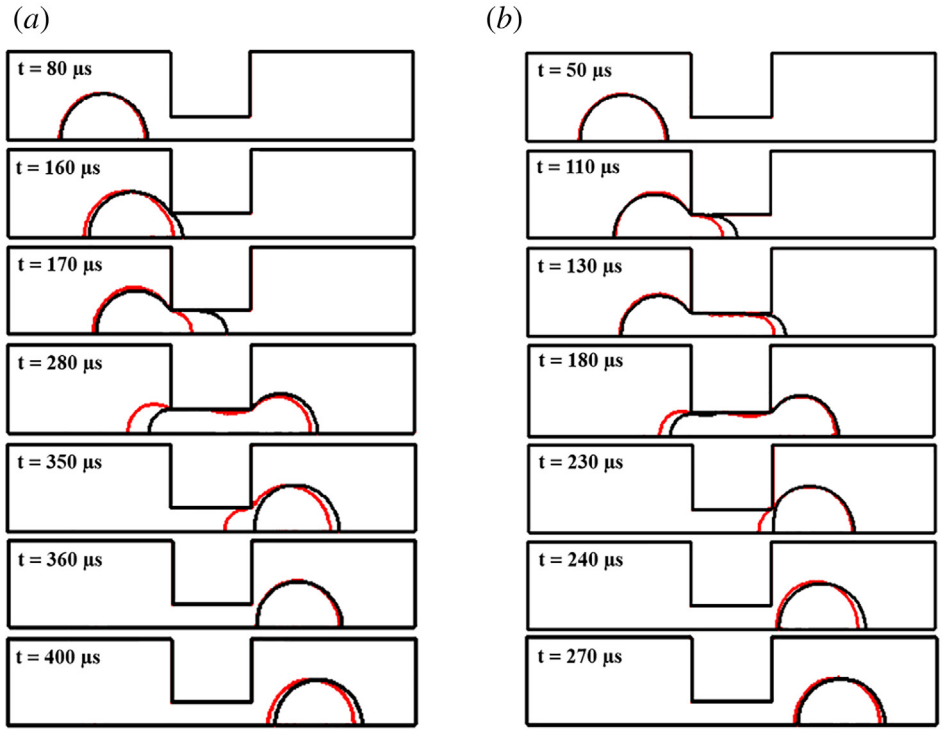

Fig. 9 Comparison of droplet shape evolutions predicted by GERRIS and ANSYS FLUENT: (*a*) $Q = 14$ nL/s and (*b*) $Q = 21$ nL/s. Black color represents droplet evolution simulated in GERRIS and red color represents for ANSYS FLUENT. The relative errors between the predicted cell elongation distances at different time instances range from 0% to 23% for $Q = 14$ nL/s and range from 0% to 7% for $Q = 21$ nL/s.

interact with the wall, and the pressure is only required to deform the outer cytoplasmic membrane. The magnitude of P_{cr} for $N/C = 0.25$ and $N/C = 0.38$ is very close (16.3 and 16.8 kPa, respectively) and is similar to that of the simple droplet model as explained in the previous works [37].

With the increase in nucleus size, P_{cr} increases due to the interaction of stiff nucleus with the filtration channel wall. In our model, the surface tension of the nuclear membrane is four times higher than the surface tension of the cytoplasmic membrane. Therefore, P_{cr} jumps to a high value with the increase of nucleus size above the filtration channel and can affect the device performance significantly by extra required pressure to let the cell pass through the filtration channel. As it is demonstrated in Fig. 11, when $N/C = 0.55$ and 0.75, the magnitude of P_{cr} is much higher compared to the $N/C = 0.25$ and 0.38 cases. Note that unlike the previous two cases, there are multiple peaks in the cell occupation stage (stages b1–b8) of the pressure profile. Equation (10) implies that surface-tension-induced pressure P_{sur} depends on the curvature of the cell and the nucleus. Dynamic behavior of the cell and the nucleus curvature during squeezing through the filtration channel causes gradual changes of P_{sur}, which is responsible for these peaks and dips in the pressure profile.

In Table 3, to investigate which pressure component is dominating, P_t is calculated using Eq. (9) for a few representative stages and compared with the values in the pressure profile. We define surface-tension-induced pressure due to the deformation of the outer cytoplasmic layer as $P_{sur,cyto,}$ and surface-tension-induced pressure due to the deformation of the nucleus as $P_{sur,nuc}$. Depending on the deformation of the cell and nucleus, P_t can be determined by $P_{sur,cyto}$, $P_{sur,nuc}$, P_{vis}, or combined effects of these components. $P_{sur,cyto}$ and $P_{sur,nuc}$ are calculated using Eq. (10). The radii of the curvature of the cell and the nucleus are measured with image processing using the best fitting arc. Note that surface-tension-induced pressure is sensitive to the curvature radius, and therefore, the calculated pressure provides a bulk estimation. For the stages of channel completely occupied by the nucleus, P_{vis} is calculated using Eq. (11) considering the viscosity of the nucleus. For most of the cases, theoretical P_t [Eq. (9)] and simulated P_t show a good agreement. At stage b1 of $N/C = 0.55$, the nucleus does not go through a significant deformation (Fig. 11(*a*)). However, calculated $P_{sur,nuc}$ is a large number due to its sensitivity to the curvature radius, which contributes to a large deviation of P_t from the simulated value. At stages b3, b5, and b6, the surface-tension-induced pressure dominates over the viscous pressure. For $N/C = 0.75$, pressure jumps to a high value due to the deformation of the nucleus and outer cytoplasmic layer. $P_{sur,nuc}$ becomes one of the dominating components of P_t when the nucleus is squeezing through the filtration channel. At stage b1, peak pressure occurs during the initial entry of the cell into the filtration channel, and P_t is majorly dominated by $P_{sur,cyto,}$ and $P_{sur,nuc}$. At stage b3, the filtration channel is occupied by the highly viscous nucleus, and therefore, P_{vis} is the dominating component of P_t. Surface-tension-induced pressure is the dominating component for the remaining two stages in the table. Where simulation results provide more insights about the physics of the squeezing process, the theory can be used for a quick estimation of the P_t and its components.

4.2 Effects of Flow Rate. The operating flow rate represents the fluid flow condition and is one of the key considerations for the design of the deformation-based microfluidic chip. In this section, we study the flow rates ranging from $Q = 7$–141 nL/s as a reasonable, practical range, and its effect on critical passing pressure for different N/C ratios. For studying the flow rates, the dimensionless Reynolds number (Re) is defined as, $e = (\rho V d/\mu)$, where ρ is the density of the cell, V is the average local velocity of the carrier flow, d is the diameter of the filtration channel, and μ is the viscosity of the carrier fluid. In Fig. 12(*a*), the flow rate is expressed in terms of nondimensional Re number and plotted in

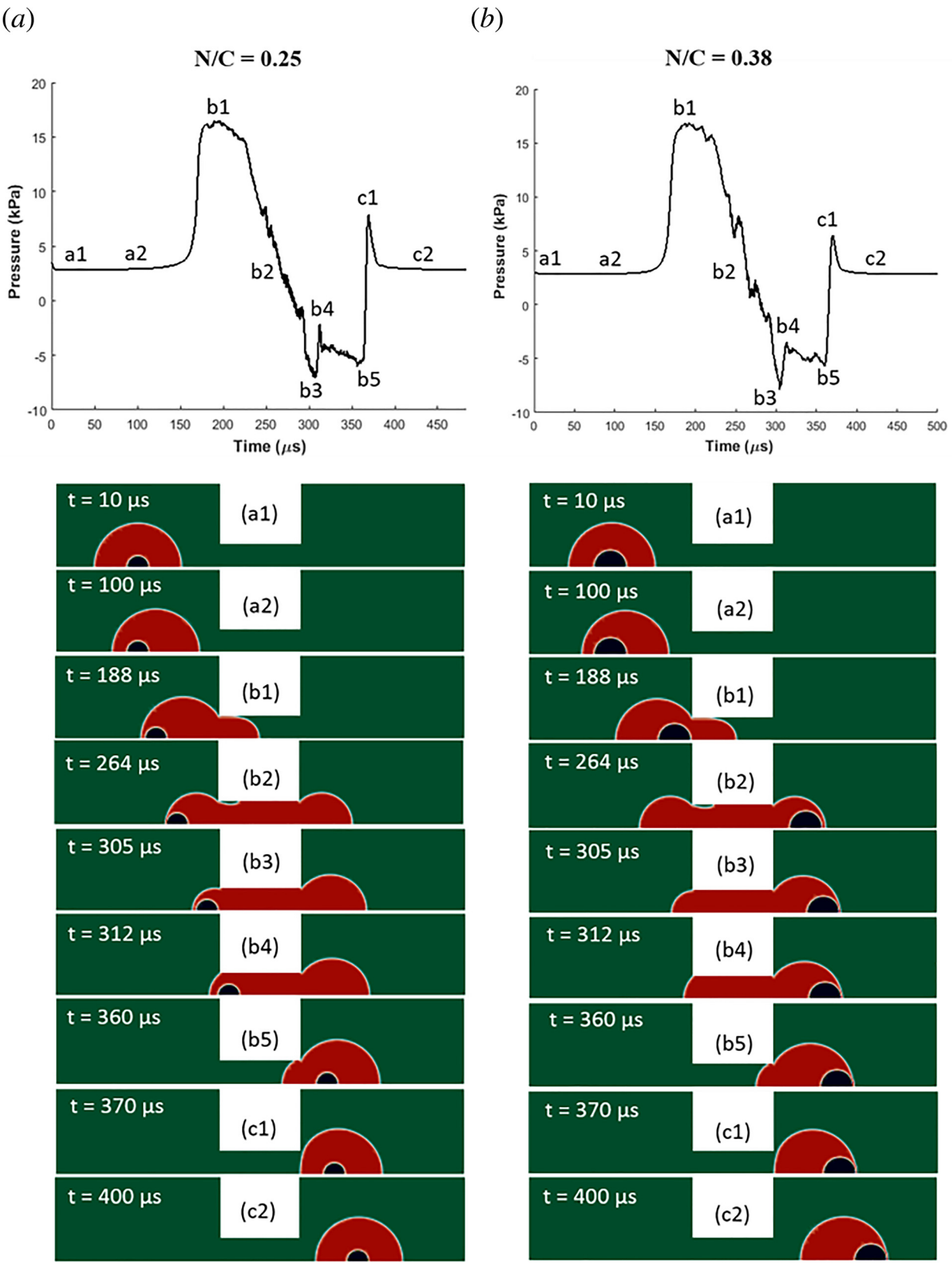

Fig. 10 Pressure profile for: (*a*) *N/C* = 0.25 and (*b*) *N/C* = 0.38 with different stages of the cell evolution during squeezing process. When the nucleus size is smaller than the filtration channel size, it results in identical pressure profiles. The smaller nucleus does not deform significantly and hence there is no direct effect of the nucleus in the pressure profile.

the x-axis. The critical pressure P_{cr} increases linearly with the increase of Re because shear force on the cell increase with the flow rate, which causes nonspherical initial aspiration of the cell. Previous studies have shown that nonspherical deformation results in a higher pressure at the entrance of the channel (28). Figure 12(*b*) demonstrates the initial aspiration of the cell for three Re numbers. It is clear that with the increase in Re, the leading edge of the cell follows parabolic deformation instead of

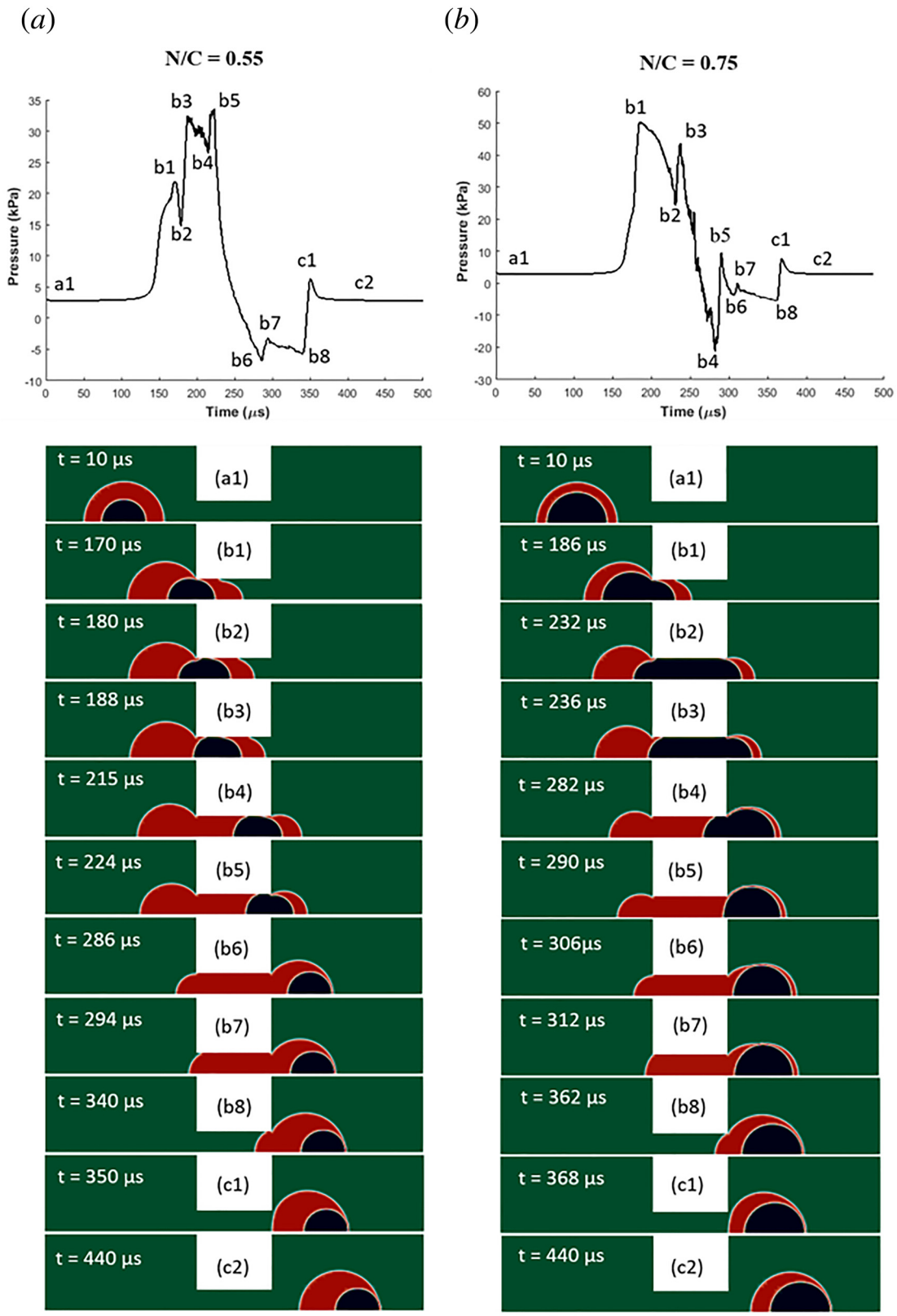

Fig. 11 Pressure profile for: (*a*) *N*/*C* = 0.55 and (*b*) *N*/*C* = 0.75. The pressure jumps to a higher value when the nucleus size is comparable or greater than the size of the filtration channel as stiffer nucleus requires higher pressure to deform and squeeze through.

spherical deformation, which causes the pressure to jump to a higher value. As we mentioned in Sec. 4.1, a nucleus smaller than the filtration channel size does not contribute significantly to the device operating pressure. Therefore, the magnitudes of P_{cr} for $N/C = 0.25$ and $N/C = 0.38$ are same for the flow rates range studied here and the two curves overlap. in contrast, for higher N/C ratio, P_{cr} jumps to higher values due to the interaction of the nucleus with the filtration channel wall. As the nucleus is stiffer than the

Table 3 Comparison of calculated and simulated pressure values at different stages of the squeezing process for the nucleus larger than the size of the filtration channel

Evolution stage	Time, t (μs)	$P_{sur,cyto}$ (Eq. (10)) kPa	$P_{sur,nuc}$ (Eq. (10)) kPa	P_{vis} (Eq. (11)) kPa	P_t (Eq. (9)) kPa	P_t (simulation) kPa
$N/C = 0.55$						
b1	170	17.9	11.9	2.2	32	21.8
b3	188	14.6	18.4	2.2	35.2	32.2
b5	224	8.1	27.8	2.2	38.1	33.6
b6	286	−8.9	0	2.2	−6.7	−6.6
$N/C = 0.75$						
b1	186	12.1	33.5	2.2	47.8	50.2
b3	236	9.1	11.8	21.2	42.1	42.4
b4	282	−4.1	−21.8	2.2	−23.7	−18.9
b8	362	−5.3	0	2.2	−3.1	−5.3

$P_{sur,cyto,}$ and $P_{sur,nuc}$ represent surface-tension-induced pressure due to the deformation of outer cytoplasmic layer and nucleus, respectively.

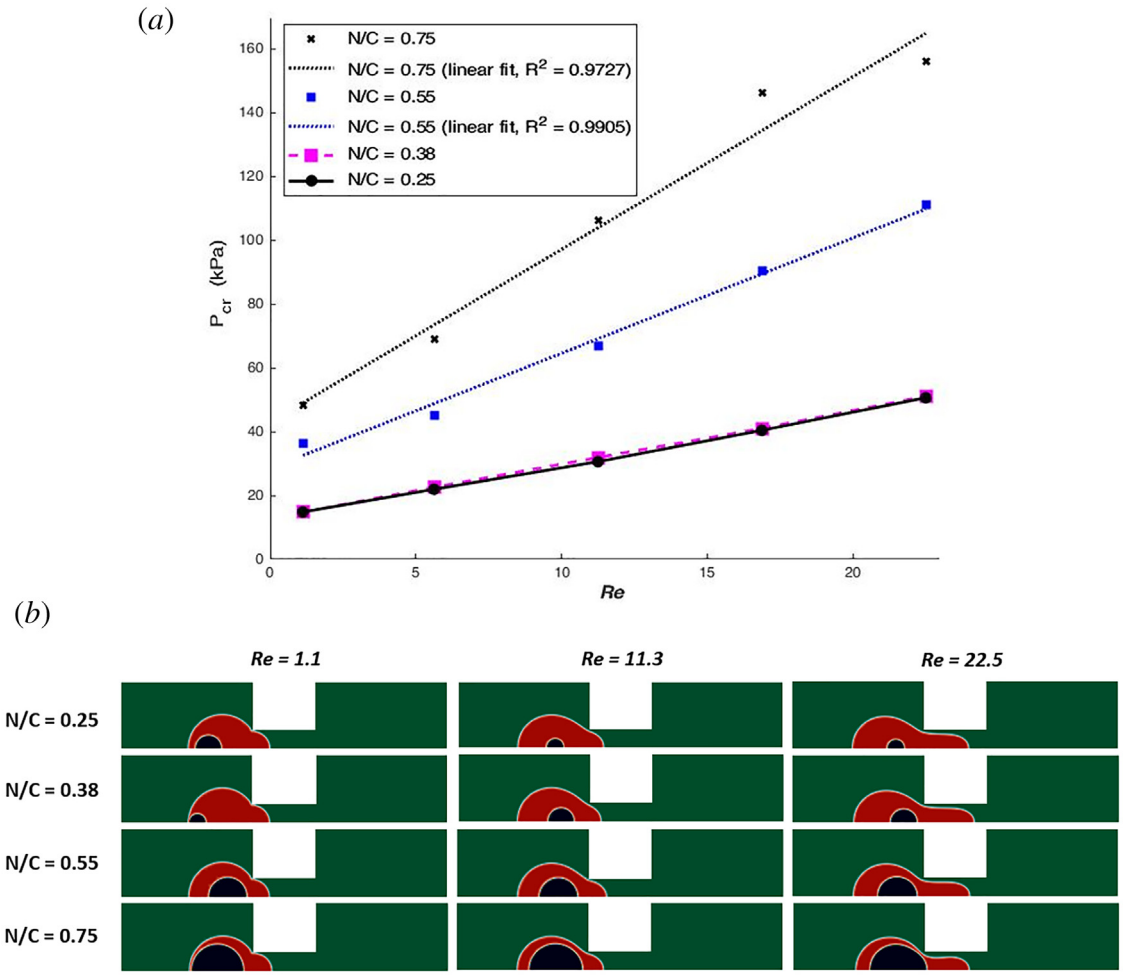

Fig. 12 (*a*) Critical pressure (P_{cr}) plotted against Re number. (*b*) Cell evolution corresponding to low (Re = 1.1), medium (Re = 11.3), and high (Re = 22.5) flow rates for different *N/C* ratios. P_{cr} increases linearly with the Re as shear force increases with flow rates. The increased shear force causes the cell to deform nonspherically during the initial aspiration, and as a result, the pressure jumps to a higher value.

cytoplasm, it requires higher pressure to deform the nucleus. In addition, when the channel is occupied by the highly viscous nucleus, viscous pressure inside the channel is also high.

Critical pressure occurs at different stages of the squeezing process, depending on the N/C ratio and position of the nucleus in the filtration channel. The stage where critical pressure occurs is termed as the critical passing stage. Figure 13 illustrates the critical passing stages for different N/C ratios corresponding to flow rates (expressed in terms of Re number). For $N/C < 0.50$, there is no contact between the nucleus and the channel wall, and P_{cr} occurs during the initial aspiration of the cytoplasm (cytoaspiration stage). As the viscosity of the cell cytoplasm is very low, P_{cr} is dominated by the surface-tension-induced pressure due to the deformation of the outer cytoplasmic layer. For $N/C > 0.50$, the P_{cr} occurs when the filtration channel is blocked by the nucleus (nucleus blocking stage) as the highly viscous and stiffer nucleus

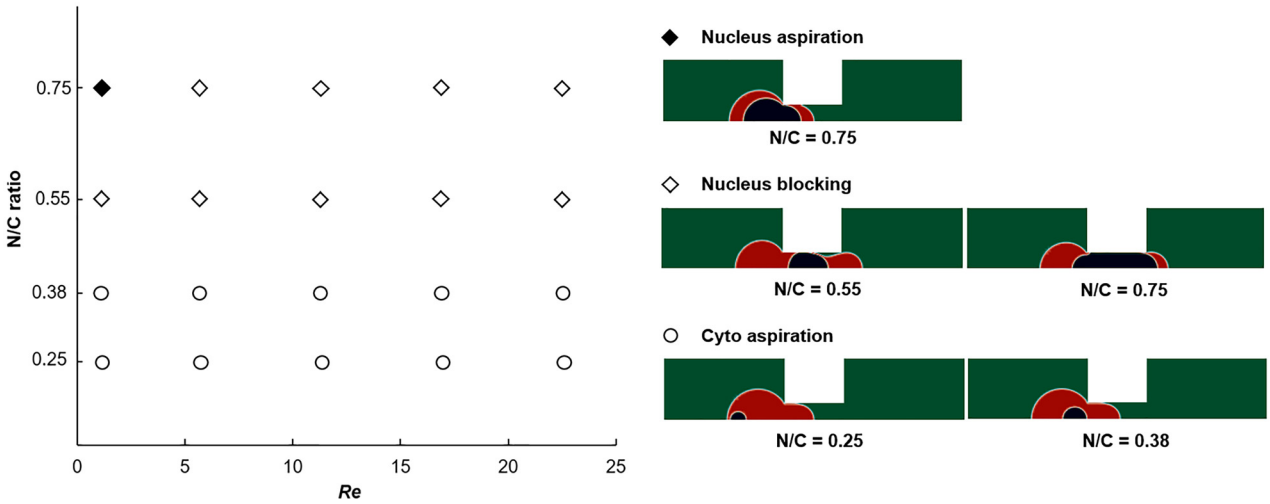

Fig. 13 Critical cell passing stages for different *N/C* ratios corresponding to flow rates (expressed in terms of Re number). The critical cell passing stage is dependent on the *N/C* ratio. In general, *N/C* < 0.50 experiences cytoaspiration and *N/C* > 0.50 experiences nucleus blocking stage.

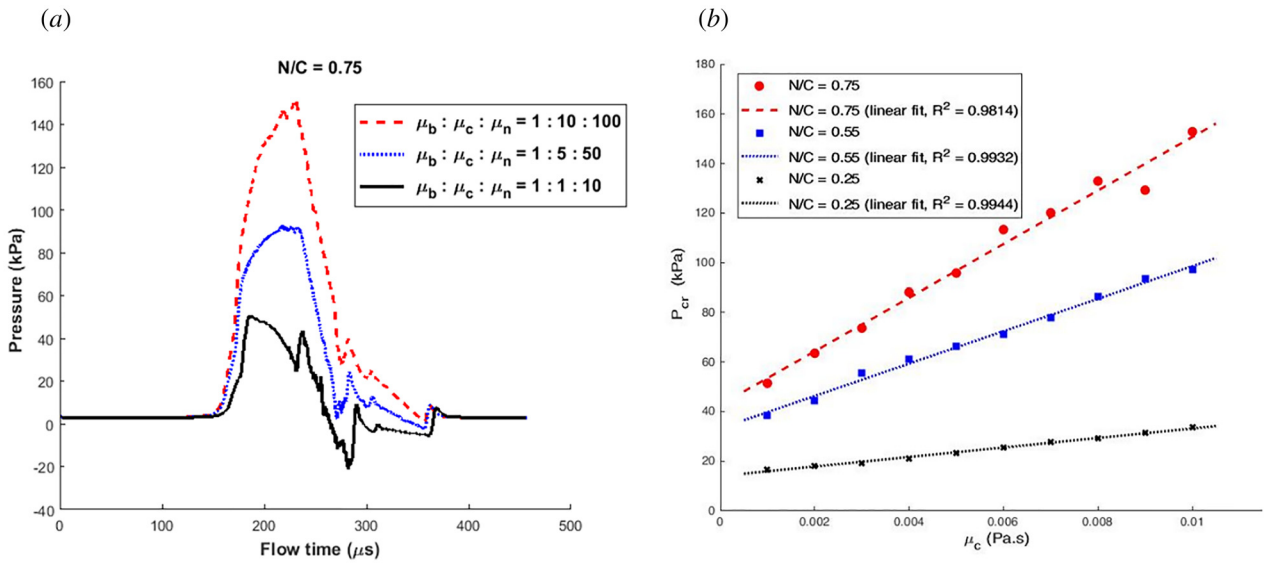

Fig. 14 (*a*) Pressure profiles for different viscosities—μ_b:μ_c:μ_n = 1:1:10, μ_b:μ_c:μ_n = 1:5:50, and μ_b:μ_c:μ_n = 1:10:100. Critical pressure rises with the increase of the cell viscosity. Cell aspiration in the filtration channel is led by surface tension and viscous force instead of ideal surface-tension-dominated aspiration only. (*b*) P_{cr} versus cell cytoplasmic viscosity (μ_c). Note that P_{cr} linearly increases with the increase of cytoplasmic viscosity (μ_c). For smaller nucleus size (i.e., *N/C* = 0.25), there is no significant impact of nucleus viscosity in the pressure profile. The viscous nucleus plays a significant role when it is larger than the channel size. Hence, the slope of the curve increases with the *N/C* ratio.

contributes to the total pressure. An exception for $N/C = 0.75$ is observed at $\mathrm{Re} = 1.1$, where P_{cr} occurs during the initial aspiration of the nucleus (nucleus aspiration stage). The reason is that combined $P_{sur,cyto}$ and $P_{sur,nuc}$ during the nucleus aspiration stage is higher than the P_{vis} in the nucleus blocking stage at the low flow rate. This study shows that the critical cell passing stage does not depend on the flow rate. Rather it depends on the N/C ratio of the droplet.

4.3 Effects of Viscosity. In this section, we study the effect of cell viscosity on the device operating pressure. Figure 14(*a*) illustrates three representative pressure profiles for low cell viscosity μ_b:μ_c:μ_n = 1:1:10, medium viscosity μ_b:μ_c:μ_n = 1:5:50, and high viscosity μ_b:μ_c:μ_n = 1:10:100 with $N/C = 0.75$. In the case of low viscosity ratio μ_b:μ_c:μ_n = 1:1:10, the P_{cr} is mainly dominated by the P_{sur} due to the deformation of the nucleus and outer cytoplasmic layer. With the increase in cell viscosity, i.e., for μ_b:μ_c:μ_n = 1:5:50 and μ_b:μ_c:μ_n = 1:10:100, the shear stress inside the cell increases, and the surface force becomes stronger to resist deformation. Therefore, the aspiration process in the filtration channel requires higher pressure to deform the cell against increased viscous force, and the cell evolution follows less spherical shape, which causes much higher surface-tension-induced pressure P_{sur}. As mentioned in Sec. 4.1, P_{cr} does not necessarily occur during the initial aspiration for all N/C ratio. Based on the shape and position of the highly viscous nucleus during the cell occupation stage, viscous pressure P_{vis} may dominate over surface-tension-induced pressure P_{sur} and determine the P_{cr}. It is clear from Fig. 14(*a*) that the dip values of the pressure profile

shift upward due to the dominance of P_{vis} over P_{sur}. Due to the increased contribution from the P_{vis}, P_{cr} jumps to a higher level for the medium and high viscosity cases. Figure 14(*b*) depicts the relationship between cell viscosity and critical pressure P_{cr}. The cell viscosity in the x-axis is expressed in terms of μ_c, as μ_n is always ten times than the μ_c. The critical pressure P_{cr} increases linearly with the increase of cytoplasm viscosity μ_c. In the case of $N/C = 0.25$, there is no direct effect from the nucleus; hence, P_{cr} increases with the increase of the cytoplasm viscosity (μ_c) mainly. The viscosity of the nucleus plays a vital role when its size is comparable or larger than the size of the filtration channel (i.e., $N/C = 0.55$ and 0.75 in our study). Note that with the increase of N/C ratio, the slope of the curves increases because a highly viscous large nucleus has more contribution in the pressure profile. For $N/C = 0.75$ as we have discussed in Sec. 4.1, critical pressure occurs when the nucleus occupies the filtration channel. With the development of higher shear stress inside the cell, it becomes more difficult for the surface force to recover the original shape of the deformed cell. As a result, P_{cr} jumps to a higher level compared to the low and medium N/C ratio.

5 Model Limitation and Future Work

In this work, we first compare our numerical results with the existing theoretical model in the literature [24,25]. Since the theoretical model assumes a spherical shape of the deformed cell, whereas the numerical simulation predicts a not so perfect spherical shape in the head and tail portions, there is some disagreement between our predicted numerical values and the theory. Nevertheless, the aforementioned comparison serves as a good starting point to evaluate the performance of the model. One limitation of our model is regarding the assumed linear elastic effect of the cortical shell [52,53]. When modeling cells that undergo large deformation, because of the sharp bend observed for cells from micropipette cell aspiration experiments, we anticipate the bending rigidity of the cortical shell to be negligibly small. Thus, the cell membrane is modeled as linear elastic as a first attempt with only in-plane stress components being considered in this work, neglecting any viscous hyperelastic or inelastic components that may arise from the fluid-like behavior of lipid bilayers. Adapting hyperelastic constitutive models with shear components may bring further insights into the cell-squeezing process although obtaining realistic rheological properties of the lipid bilayer cell membrane for such constitutive models may present a challenge. In addition, the complex cell-squeezing process may involve the emergence of a dynamic thin lubricating layer which may strongly affect the obtained numerical results. The AMR approach used in this work is a good choice as such thin layers are challenging to resolve in fixed-grid simulations. Future work may consider including thin lubricating boundary layers in the numerical model to enhance the prediction of resistance to cell motion in narrow channels. The 2D axisymmetric model may not reveal all aspects of the cell entry, such as the off-center entrance of the cell through the microfiltration. However, since in this study, our focus is to enhance the physiological accuracy of our model, the off-center effect can be disregarded, and 2D axisymmetric model can be used to capture the downstream fluid field variables. Finally, wall shear stress has also shown to have a significant effect on the cell viability on the deformability-based CTC separation devices [54]. Zhang et al. [37] have previously demonstrated that the thin film formed between the cell and channel wall dominates the flow characteristics such as shear stress and pressure distribution in the filtration channel. However, still the effect of the nucleus on fluid dynamic variables inside the microfilter is unknown and can be a topic of future studies.

6 Conclusion

In this study, the AMR-based numerical method is used to simulate the droplet dynamics during passing through the microfilter. As the living cells are heterogeneous in nature with a nucleus occupying a large percentage of the cell volume, we model the CTC as a compound droplet to investigate the deformability behavior during the squeezing process more realistically. The effects of different parameters (nuclear-to-cytoplasmic size ratio or N/C ratio, flow rate, and cell viscosity on the cell behavior and microfiltration process) are studied in detail. For nucleus size smaller than the filtration channel ($N/C < 0.50$), the cell behaves like a simple droplet consisting of a homogeneous fluid encapsulated by a cortical membrane. When the stiffer and highly viscous nucleus is larger than the filtration channel size ($N/C > 0.50$), the pressure profile is greatly influenced. The dynamic variation of the nucleus curvature results in multiple peaks and dips in the pressure profile. Depending on the size and position of the nucleus during the squeezing process, total pressure can be dominated by either the surface-tension-induced pressure or the viscous pressure. Then, we study the effects of different operating flow rates and cell viscosity in the device operating pressure. Our study shows that critical pressure follows a linear trend with the flow rates and cell viscosity irrespective of the N/C ratios. Typically, critical pressure for $N/C < 0.50$ occurs during the initial cytoaspiration stage, whereas for $N/C > 0.50$, it occurs at the nucleus blocking stage. For smaller nucleus, there is no direct effect from the nucleus viscosity on the critical pressure. When the nucleus is comparable to the channel size or larger, the contribution of viscous pressure due to the highly viscous nucleus is significant, and the critical pressure jumps to a high value. These findings, along with the proposed approach, offer insights into the CTC filtration process and may aid in the design of future microfluidic chips.

Funding Data

- National Science Foundation (Award No. NSF ECCS-1917299; Funder ID: 100000148/100000001).

References

[1] Liberko, M., Kolostova, K., and Bobek, V., 2013, "Essentials of Circulating Tumor Cells for Clinical Research and Practice," Crit. Rev. Oncol. Hematol., **88**(2), pp. 338–356.

[2] Autebert, J., Coudert, B., Bidard, F.-C., Pierga, J.-Y., Descroix, S., Malaquin, L., and Viovy, J.-L., 2012, "Microfluidic: An Innovative Tool for Efficient Cell Sorting," Methods, **57**(3), pp. 297–307.

[3] Aghilinejad, A., Aghaamoo, M., and Chen, X., 2019, "On the Transport of Particles/Cells in High-Throughput Deterministic Lateral Displacement Devices: Implications for Circulating Tumor Cell Separation," Biomicrofluidics, **13**(3), p. 034112.

[4] Dincau, B. M., Aghilinejad, A., Hammersley, T., Chen, X., and Kim, J.-H., 2018, "Deterministic Lateral Displacement (DLD) in the High Reynolds Number Regime: High-Throughput and Dynamic Separation Characteristics," Microfluid. Nanofluid., **22**(6), p. 59.

[5] Aghaamoo, M., Zhang, Z. F., Chen, X. L., and Xu, J., 2015, "Deformability-Based Circulating Tumor Cell Separation With Conical-Shaped Microfilters: Concept, Optimization, and Design Criteria," Biomicrofluidics, **9**(3), p. 034106.

[6] Chang, P., Hashem, M. A., Chen, X., and Tan, H., 2019, "Dynamics of Compound Droplet Passing Through a Conical CTC Microfilter," ASME Paper No. IMECE2019-10519.

[7] Yamada, M., Nakashima, M., and Seki, M., 2004, "Pinched Flow Fractionation: Continuous Size Separation of Particles Utilizing a Laminar Flow Profile in a Pinched Microchannel," Anal. Chem., **76**(18), pp. 5465–5471.

[8] Tanaka, T., Ishikawa, T., Numayama-Tsuruta, K., Imai, Y., Ueno, H., Matsuki, N., and Yamaguchi, T., 2012, "Separation of Cancer Cells From a Red Blood Cell Suspension Using Inertial Force," Lab Chip, **12**(21), pp. 4336–4343.

[9] Zborowski, M., and Chalmers, J. J., 2011, "Rare Cell Separation and Analysis by Magnetic Sorting," Anal. Chem., **83**(21), pp. 8050–8056.

[10] Augustsson, P., Magnusson, C., Nordin, M., Lilja, H., and Laurell, T., 2012, "Microfluidic, Label-Free Enrichment of Prostate Cancer Cells in Blood Based on Acoustophoresis," Anal. Chem., **84**(18), pp. 7954–7962.

[11] MacDonald, M. P., Spalding, G. C., and Dholakia, K., 2003, "Microfluidic Sorting in an Optical Lattice," Nature, **426**(6965), pp. 421–424.

[12] Aghilinejad, A., Aghaamoo, M., Chen, X., and Xu, J., 2018, "Effects of Electrothermal Vortices on Insulator-Based Dielectrophoresis for Circulating Tumor Cell Separation," Electrophoresis, **39**(5–6), pp. 869–877.

[13] Aghaamoo, M., Aghilinejad, A., and Chen, X., 2017, "Numerical Study of Insulator-Based Dielectrophoresis Method for Circulating Tumor Cell Separation," Microfluid., BioMEMS, Med. Microsyst. XV, **10061**, p. 100611A.

[14] Aghaamoo, M., Aghilinejad, A., Chen, X., and Xu, J., 2019, "On the Design of Deterministic Dielectrophoresis for Continuous Separation of Circulating

Tumor Cells From Peripheral Blood Cells," Electrophoresis, **40**(10), pp. 1486–1493.
[15] Gossett, D. R., Weaver, W. M., Mach, A. J., Hur, S. C., Tse, H. T. K., Lee, W., Amini, H., and Di Carlo, D., 2010, "Label-Free Cell Separation and Sorting in Microfluidic Systems," Anal. Bioanal. Chem., **397**(8), pp. 3249–3267.
[16] Denais, C. M., Gilbert, R. M., Isermann, P., McGregor, A. L., Te Lindert, M., Weigelin, B., Davidson, P. M., Friedl, P., Wolf, K., and Lammerding, J., 2016, "Nuclear Envelope Rupture and Repair During Cancer Cell Migration," Science, **352**(6283), pp. 353–358.
[17] Ishikawa, T., Fujiwara, H., Matsuki, N., Yoshimoto, T., Imai, Y., Ueno, H., and Yamaguchi, T., 2011, "Asymmetry of Blood Flow and Cancer Cell Adhesion in a Microchannel With Symmetric Bifurcation and Confluence," Biomed. Microdev., **13**(1), pp. 159–167.
[18] Lim, C., Zhou, E., and Quek, S., 2006, "Mechanical Models for Living Cells—A Review," J. Biomech., **39**(2), pp. 195–216.
[19] Bronzino, J. D., and Peterson, D. R., 2014, *Biomedical Engineering Fundamentals*, CRC Press, Boca Raton, FL.
[20] Evans, E., and Yeung, A., 1989, "Apparent Viscosity and Cortical Tension of Blood Granulocytes Determined by Micropipet Aspiration," Biophys. J., **56**(1), pp. 151–160.
[21] Evans, E., and Kukan, B., 1984, "Passive Material Behavior of Granulocytes Based on Large Deformation and Recovery After Deformation Tests," Blood, **64**(5), pp. 1028–1035.
[22] Bagnall, J. S., Byun, S., Begum, S., Miyamoto, D. T., Hecht, V. C., Maheswaran, S., Stott, S. L., Toner, M., Hynes, R. O., and Manalis, S. R., 2015, "Deformability of Tumor Cells Versus Blood Cells," Sci. Rep., **5**(1), p. 18542.
[23] Leong, F. Y., Li, Q., Lim, C. T., and Chiam, K.-H., 2011, "Modeling Cell Entry Into a Micro-Channel," Biomech. Model. Mechanobiol., **10**(5), pp. 755–766.
[24] Zhang, Z., Xu, J., Hong, B., and Chen, X., 2014, "The Effects of 3D Channel Geometry on CTC Passing Pressure–Towards Deformability-Based Cancer Cell Separation," Lab Chip, **14**(14), pp. 2576–2584.
[25] Zhang, Z., Chen, X., and Xu, J., 2015, "Entry Effects of Droplet in a Micro Confinement: Implications for Deformation-Based Circulating Tumor Cell Microfiltration," Biomicrofluidics, **9**(2), p. 024108.
[26] Dong, C., Skalak, R., and Sung, K.-L. P., 1991, "Cytoplasmic Rheology of Passive Neutrophils," Biorheology, **28**(6), pp. 557–567.
[27] Hashem, M. A., Chen, X., and Tan, H., 2019, "An Adaptive Mesh Refinement Based Simulation for Pressure-Deformability Analysis of a Circulating Tumor Cell," Proc. SPIE, 10875, p. 108750L.
[28] Tsai, M. A., Frank, R. S., and Waugh, R. E., 1993, "Passive Mechanical Behavior of Human Neutrophils: Power-Law Fluid," Biophys. J., **65**(5), pp. 2078–2088.
[29] Zhang, X., Hashem, M. A., Chen, X., and Tan, H., 2018, "On Passing a non-Newtonian Circulating Tumor Cell (CTC) Through a Deformation-Based Microfluidic Chip," Theor. Comput. Fluid Dyn., **32**(6), pp. 753–764.
[30] Schmid-Schonbein, G., Shih, Y. Y., and Chien, S., 1980, "Morphometry of Human Leukocytes," Blood, **56**(5), pp. 866–875.
[31] Guilak, F., Tedrow, J. R., and Burgkart, R., 2000, "Viscoelastic Properties of the Cell Nucleus," Biochem. Biophys. Res. Commun., **269**(3), pp. 781–786.
[32] Luo, Z. Y., He, L., and Bai, B. F., 2015, "Deformation of Spherical Compound Capsules in Simple Shear Flow," J. Fluid Mech., **775**, pp. 77–104.
[33] Smith, K., Ottino, J. M., and de la Cruz, M. O., 2004, "Encapsulated Drop Breakup in Shear Flow," Phys. Rev. Lett., **93**(20), p. 204501.
[34] Qu, X., and Wang, Y., 2012, "Dynamics of Concentric and Eccentric Compound Droplets Suspended in Extensional Flows," Phys. Fluids, **24**(12), p. 123302.
[35] Wang, J., Xu, S., Huang, Y., and Guan, J., 2018, "Mechanical Mechanisms of the Directional Shift and Inverse of the Eccentric Compound Droplet," Phys. Fluids, **30**(4), p. 042005.
[36] Zhou, C., Yue, P., and Feng, J. J., 2008, "Deformation of a Compound Drop Through a Contraction in a Pressure-Driven Pipe Flow," Int. J. Multiphase Flow, **34**(1), pp. 102–109.
[37] Zhang, X., Chen, X., and Tan, H., 2017, "On the Thin-Film-Dominated Passing Pressure of Cancer Cell Squeezing Through a Microfluidic CTC Chip," Microfluid. Nanofluid., **21**(9), p. 146.
[38] Popinet, S., 2009, "An Accurate Adaptive Solver for Surface-Tension-Driven Interfacial Flows," J. Comput. Phys., **228**(16), pp. 5838–5866.
[39] Brackbill, J. U., Kothe, D. B., and Zemach, C., 1992, "A Continuum Method for Modeling Surface Tension," J. Comput. Phys., **100**(2), pp. 335–354.
[40] Cummins, S. J., Francois, M. M., and Kothe, D. B., 2005, "Estimating Curvature From Volume Fractions," Comput. Struct., **83**(6–7), pp. 425–434.
[41] Aulisa, E., Manservisi, S., Scardovelli, R., and Zaleski, S., 2007, "Interface Reconstruction With Least-Squares Fit and Split Advection in Three-Dimensional Cartesian Geometry," J. Comput. Phys., **225**(2), pp. 2301–2319.
[42] Scardovelli, R., and Zaleski, S., 2000, "Analytical Relations Connecting Linear Interfaces and Volume Fractions in Rectangular Grids," J. Comput. Phys., **164**(1), pp. 228–237.
[43] Popinet, S., 2003, "Gerris: A Tree-Based Adaptive Solver for the Incompressible Euler Equations in Complex Geometries," J. Comput. Phys., **190**(2), pp. 572–600.
[44] Khokhlov, A. M., 1998, "Fully Threaded Tree Algorithms for Adaptive Refinement Fluid Dynamics Simulations," J. Comput. Phys., **143**(2), pp. 519–543.
[45] Tan, H., 2016, "An Adaptive Mesh Refinement Based Flow Simulation for Free-Surfaces in Thermal Inkjet Technology," Int. J. Multiphase Flow, **82**, pp. 1–16.
[46] Tan, H., 2017, "Numerical Study on Splashing of High-Speed Microdroplet Impact on Dry Microstructured Surfaces," Comput. Fluids, **154**, pp. 142–166.
[47] Preetha, A., Huilgol, N., and Banerjee, R., 2005, "Interfacial Properties as Biophysical Markers of Cervical Cancer," Biomed. Pharmacother., **59**(9), pp. 491–497.
[48] Rejniak, K. A., 2012, "Investigating Dynamical Deformations of Tumor Cells in Circulation: Predictions From a Theoretical Model," Front. Oncol., **2**, p. 111.
[49] Marella, S. V., and Udaykumar, H., 2004, "Computational Analysis of the Deformability of Leukocytes Modeled With Viscous and Elastic Structural Components," Phys. Fluids, **16**(2), pp. 244–264.
[50] Bruus, H., 2008, *Theoretical Microfluidics*, Oxford University Press, Oxford, UK.
[51] Gonzalez-Rodriguez, D., Guillou, L., Cornat, F., Lafaurie-Janvore, J., Babataheri, A., de Langre, E., Barakat, A. I., and Husson, J., 2016, "Mechanical Criterion for the Rupture of a Cell Membrane Under Compression," Biophys. J., **111**(12), pp. 2711–2721.
[52] Raj, A., and Sen, A., 2018, "Entry and Passage Behavior of Biological Cells in a Constricted Compliant Microchannel," RSC Adv., **8**(37), pp. 20884–20893.
[53] Savin, T., Bandi, M., and Mahadevan, L., 2016, "Pressure-Driven Occlusive Flow of a Confined Red Blood Cell," Soft Matter, **12**(2), pp. 562–573.
[54] Aghilinejad, A., Landry, C., Cha, G., and Chen, X., "Enhancing the Cell Viability in High Throughput Deterministic Lateral Displacement Separation of Circulating Tumor Cells," ASME Paper No. IMECE2019-10209.